

Satellite observation of coal mining subsidence by persistent scatterer analysis

Hahn Chul Jung^{a,1}, Sang-Wan Kim^b, Hyung-Sup Jung^a,
Kyung Duck Min^a, Joong-Sun Won^{a,*}

^a Department of Earth System Sciences, Yonsei University, 134 Sinchon-Dong, Seodaemun-Gu, Seoul 120-749, Republic of Korea

^b Department of Geoinformation Engineering, Sejong University, Seoul, Republic of Korea

Received 5 November 2006; received in revised form 13 February 2007; accepted 27 February 2007

Available online 12 April 2007

Abstract

Ground subsidence persistently occurs in abandoned coal mining areas. This paper presents an investigation of ground subsidence measurement using persistent scatterers recorded by space-borne synthetic aperture radar (SAR). During the period from November 1992 to October 1998, twenty-five JERS-1 SAR interferometric pairs were obtained and used to measure subsidence in the Gaeun coal mining area, Korea. To validate the subsidence estimated by the persistent scatterers SAR interferometry (PS technique), the results were compared with the degree of crack level obtained by a 1997 field survey. The study area was divided into five classes based on measured crack levels. The line-of-sight (LOS) subsidence rate of each group was estimated by the phase of 135 scatterers selected from the five classes. The maximum subsidence was measured by radar as 11.2 cm over 6 yr. The mean subsidence rate of one class was found to be 0.5 cm/yr where cracks most severely developed. The radar-estimated subsidence agrees well with the degree of crack level. The PS technique is useful for the measurement of ground subsidence in abandoned coal mining areas, even in mountainous regions.

© 2007 Elsevier B.V. All rights reserved.

Keywords: SAR interferometry; Mining subsidence; Persistent scatterers; Crack level; JERS-1

1. Introduction

The exploitation of underground natural resources often causes persistent land subsidence, ranging from small scale collapses to regional settlements. The subsidence rate varies with geological characteristics and the mechanical properties of rocks. Subsidence associated

with abandoned mines can cause many problems, such as building collapse, road damage, environmental pollution, etc. Careful monitoring and modeling of subsidence has been conducted in efforts to prevent associated disasters (Steve and Kuipers, 2002). The majority of subsidence surveys have been conducted over limited, high-risk areas on a point-by-point basis using ground leveling and GPS techniques with accuracies of a few millimeters (Demoulin et al., 2005). However, these field surveys are time consuming, labor-intensive and costly. The dynamics of mining subsidence are difficult to model. Model parameters include seam thickness, mining depth, and oft inaccurate measurements of seam gradient and direction (Wright and Stow, 1999).

* Corresponding author. Tel.: +82 2 2123 2673; fax: +82 2 313 2549.
E-mail address: jswon@yonsei.ac.kr (J.-S. Won).

¹ H. C. Jung is now with the School of Earth Sciences, The Ohio State University, 275 Mendenhall Laboratory 125 South Oval Mall, Columbus, OH 43210-1308, USA.

Using space-borne synthetic aperture radar (SAR) data, differential SAR interferometry (DInSAR) may be used to monitor centimeter-scale surface displacements over large geographic extents. SAR interferometry has the advantage, compared to traditional subsidence survey methods, of improving subsidence model accuracy by vastly increasing the quantity of available feedback data (Wright and Stow, 1999). The phase difference of two complex SAR images in the same area is a function of topography and ground displacement. The topographic phase term can be easily eliminated with orbit data and topographic information. The resultant image is a differential SAR interferogram that provides information regarding ground displacements. It has been applied successfully to the measurement of subtle crustal deformations caused by earthquakes (Massonnet et al., 1993) and volcanoes (Jonsson et al., 1999), or by human activities such as ground water pumping (Sneed et al., 2001), mining (Carnece and Delacourt, 2000), the reclamation of coastal land (Kim et al., 2005) and water level changes (Alsdorf et al., 2000). However, this method has limitations such as decorrelation noise caused by random temporal variations of terrain reflectivity and atmospheric noise related to random fluctuations of atmospheric refraction (Berardino et al., 2003). To overcome such limitations, the permanent scatterers SAR interferometry (PSInSAR) technique has more recently been employed in the monitoring of slow but consistent ground subsidence (Ferretti et al., 2000). The PSInSAR technique allows highly accurate measurements of deformation that occurs at individual, phase-dependent radar targets called permanent or persistent scatterers (PS). PSs are not affected by either geometrical or temporal decorrelation, and they can be identified by statistically analyzing their amplitude and phase returns (Colesanti et al., 2001). Although this technique requires the situation of persistent scatterers in the area of investigation, as well as iterative images of the area, it has the advantages of having fewer limitations on baseline and temporal decorrelation, a reliable correction for atmospheric effects, and easier time series analysis (Colesanti et al., 2003). In this paper, a persistent scatterers technique (PS technique) is applied to the measurement of subsidence from an abandoned coal mine in a mountainous region.

Most abandoned mines in Korea are located in mountainous areas. It is especially difficult to apply SAR interferometry to mountainous regions, where the branches and leaves of dense vegetation cause volume scattering, resulting in severe temporal decorrelation. Traditional DInSAR is not suitable for the measurement of ground subsidence in sites that commonly experience

high temporal decorrelation. In addition, subsidence in coal mines is generally characterized by localized damages accompanied by small scale collapse. Given the advantages of the PS technique, it is expected to more effectively detect subsidence in mountainous regions, such as the study area investigated herein. PS technique enables the detection and measurement of subsidence at a point, that is, at the single-pixel resolution. The objective of this study is to produce ground subsidence information and maps from SAR-derived data. To validate the performance of the PS technique, the subsidence rates of surfaces above abandoned coal mines in Gaeun, Korea, are measured and compared with ground-truthed crack levels obtained by field survey.

The remainder of the paper is organized as follows. Section 2 describes the study area and the JERS-1 SAR interferometric pairs used to measure ground subsidence. Section 3 details the method to analyze persistent scatterers. Section 4 presents and discusses various aspects of the results, and conclusions are offered in Section 5.

2. Study area and data

2.1. Study area

More than 300 coal mines have been abandoned in Korea since 1989, and it has become necessary to monitor surface deformation in those areas. The study area, located in Gaeun, Korea, is approximately 1×1 km (Fig. 1). The Yangsancheon River runs, which is about 30–70 m wide, bisects the eastern portion of the town. Hills and mountains with slopes of 30–45° flank the town's northeast and southwest margins. The area has three abandoned coal mines; the first and second Gaeun Mines were abandoned in 1976, and the Taeyang Mine was deserted in 1991. The geologic formations explored for coal include Kumchon/Pamchi and Changsong Formations, formed during the Carboniferous and Permian periods. The Kumchon and Pamchi Formations consist mainly of shale, sandstone and two to three lenticular limestone beds. The Changsong Formation consists of alternating beds of sandstone and shale.

Subsidence is known to be triggered by two phenomena: calcite dissolution and the abandonment of coal mines. Calcite dissolution has been shown to be accelerated by groundwater present near thrust zones. Subsidence originated from calcite dissolution is generally characterized by the abrupt formation of local depressions. In this study, we measure the slow but continuous subsidence associated with abandoned coal mines, as it is difficult to detect sudden collapses by means of persistent scatter analysis.

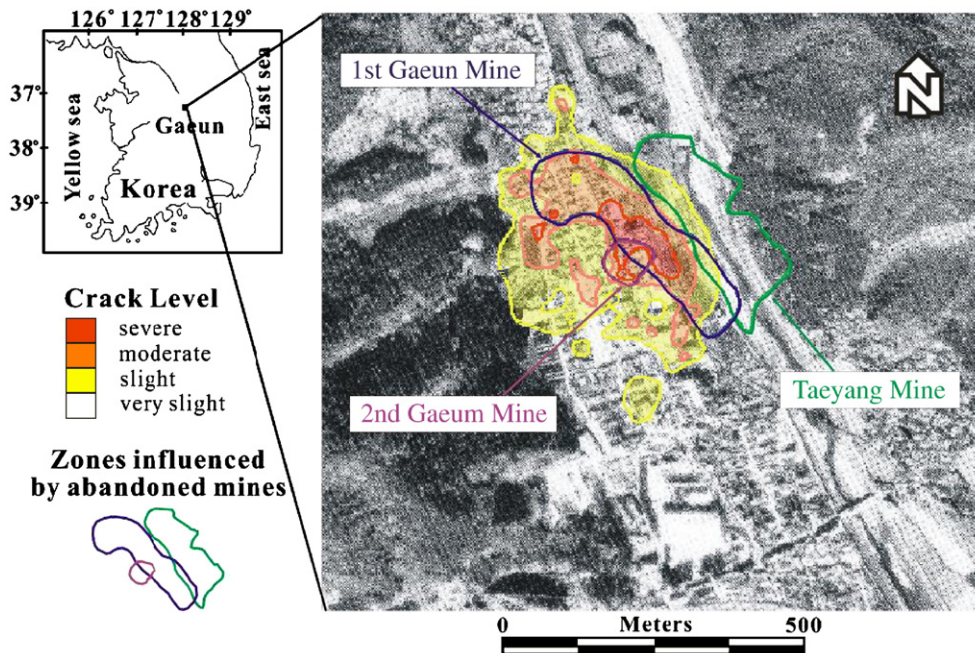


Fig. 1. Location map and aerial photograph of the study area overlaid with influenced zones of the abandoned mines and the degree of crack level. The crack levels were obtained by 1997 field surveys. The blue polygon indicates the zone influenced by the first Gaeun Mine, the violet polygon indicates that influence by the second Gaeun Mine, and the green polygon indicates that influenced by the Taeyang Mine.

In 1997, the Coal Industry Promotion Board of Korea (Coal Industry Promotion Board, 1997) surveyed the degree of crack level in Gaeun to assess local ground stability following standards suggested by the NCB (1975) and Bruhn et al. (1983). The influence zones of the abandoned mines and the degree of crack level are superimposed on the aerial photo in Fig. 1. The degree of crack level is defined by the measurement of crack widths on man made structures, and is considered ‘severe’ if over 15 mm, ‘moderate’ if between 5 and 15 mm, ‘slight’ if less than 5 mm, and ‘very slight’ less than 1 mm. To validate the utility of the PS technique application, the degree of crack level from the 1997 survey will be compared with the radar-measured subsidence rates. The survey was limited to man-made structures; natural ground and residential road subsidences were not considered.

2.2. Description of datasets

Twenty-six JERS-1 SAR images were collected from November 1992 to October 1998 in the Gaeun area, and were co-registered to a master image acquired on 27 October 1996. From the SAR datasets, a total of 25 JERS-1 SAR interferometric pairs were constructed as listed in Table 1. In order to overcome the ambiguity of the JERS-1 orbit, inaccurate orbits were corrected by orbit modeling with SAR images and ground control

points. Modeling was performed by matching the SAR image to a simulated SAR image derived from a digital elevation model (DEM) (Kim, 2004). The 10 m DEM was constructed by interpolating 1:25,000 digital contour maps with as a triangular irregular network.

Some interferometric pairs were of low quality due to severe temporal decorrelation, geometric decorrelation and atmospheric decorrelation. The mean coherence of the constructed interferograms ranged from 0.21 to 0.39, and only 6 out of 25 pairs had a mean coherence higher than 0.3. The pairs with low coherence were, however, still useful for PS technique, which isolates stable radar targets and analyzes interferograms at stable points, yielding displacement over time (Suzanne and Sandwell, 2003). The minimum and maximum perpendicular baselines were 270 m and 3366 m, respectively, far below the critical baseline of 6 km. Perpendicular baselines of 10 pairs were larger than 1500 m. It is usually difficult to unwrap the phase from pairs with low coherence and a larger baseline. However, since only persistent scatterers were searched and used for this study, interferograms with larger baselines were kept in the dataset.

3. Persistent scatterer analysis

While traditional DInSAR utilizes single interferometric SAR pairs, different techniques exploiting time series

Table 1
Summary of the JERS-1 SAR interferometric pairs used in this study

No.	SAR image		Perpendicular baseline (ambiguity height) [m]	Time interval [days]	Coherence
	Master	Slave			
1		92/11/05	982.3 (−56.0)	−1452	0.27
2		92/12/19	462.2 (−121.1)	−1408	0.30
3		93/03/17	554.5 (−98.9)	−1320	0.29
4		93/06/13	−635.8 (86.0)	−1232	0.28
5		93/07/27	1002.5 (−54.6)	−1188	0.27
6		93/09/09	1285.6 (−42.6)	−1144	0.27
7		93/10/23	1034.8 (−52.9)	−1100	0.29
8		93/12/06	2117.1 (−25.8)	−1056	0.24
9		94/01/19	1464.7 (−37.4)	−1012	0.27
10		95/02/19	−2399.9 (22.8)	−616	0.24
11		96/03/21	−1309.4 (41.7)	−220	0.30
12	96/10/27	96/07/31	270.1 (−204.1)	−88	0.39
13		96/12/10	1271.0 (−43.0)	44	0.33
14		97/01/23	800.6 (−68.3)	88	0.33
15		97/03/08	546.3 (−101.0)	132	0.38
16		97/06/04	488.9 (−115.7)	220	0.35
17		97/10/14	−3366.1 (16.3)	352	0.21
18		97/11/27	−2210.7 (24.9)	396	0.25
19		98/01/10	−1912.0 (28.9)	440	0.26
20		98/02/23	−2389.2 (22.9)	484	0.25
21		98/04/08	3181.7 (17.2)	528	0.21
22		98/05/22	571.9 (−135.4)	572	0.31
23		98/07/05	−3042.4 (18.0)	616	0.21
24		98/08/18	−1895.3 (28.9)	660	0.26
25		98/10/01	−1557.8 (35.4)	704	0.28

of SAR data have been proposed (Ferretti et al., 2000; Bernardino et al., 2002; Usai, 2003). Persistent scatterer analysis investigates phase information of individual objects maintaining temporally stable phase. Thus, where persistent scatterers exist, a spatio-temporal phase analysis can be performed. The theoretical background is described in detail by Ferretti et al. (2000, 2001).

Fig. 2 illustrates a generalization of processing steps employed in this study. As the first step, persistent scatterer candidates are selected, followed by differential interferogram correction, persistent scatterer identification, and the estimation of the two-dimensional subsidence field. Coherence and amplitude variation is used for persistent scatterer candidate selection. Prior to identifying persistent scatterers, residual orbital fringes arising from an imprecise orbit, as well as the atmospheric effects of differential interferograms, are corrected with modeling derived from persistent scatterer candidates. At least three to four persistent scatterer candidates per square kilometer are required to perform a reliable model (Colesanti et al., 2003). A unique processing of the proposed method is to utilize coherence value to select persistent scatter candidates as well as amplitude dispersion index and to produce a subsidence

field by two-dimensional interpolation of the estimated velocities at the identified persistent scatterers. Each of the steps adopted herein are detailed in the following sub-sections.

3.1. Persistent scatterer candidate selection

Persistent scatterer candidates (PSCs) are a subset of all PSs and are used to estimate correction parameters for interferograms. We selected PSCs for their coherence to each pixel, as well as for their amplitude dispersion index. The amplitude dispersion index was first calculated in the area of interest. To compute the amplitude dispersion index (D_A), all amplitude images are stacked and the mean (m_A) and standard deviation (σ_A) of the stacked image are calculated (Ferretti et al., 2001). The amplitude dispersion index at each pixel is given by

$$D_A = \sigma_A / m_A. \quad (1)$$

The amplitude dispersion index represents stability of the ground object in terms of radar backscattering power, and smaller values are favorable for PSCs. A target with a low amplitude dispersion index smaller than a given threshold is considered as a PSC. It was proven by numerical simulation that phase standard deviation was as low as the amplitude dispersion index if targets had a low amplitude dispersion index less than 0.25 (Ferretti et al., 2001).

Provided that the signal-to-noise ratio (SNR) is high enough, a measure of phase stability can be obtained from the amplitude dispersion index alone. However, JERS-1 SAR data generally have low SNRs, and their amplitude dispersion index is often not good enough to serve as a single criterion for PSC selection. For this reason, coherence (γ) maps calculated by a kernel of 9×3 pixels in azimuth and range were used as complementary data to aid in the selection of reliable PSCs. Coherence is a measure of the phase consistency in radar return between two images, and is defined by (Zebker and Villasenor, 1992)

$$\gamma = \frac{\langle s_1 \cdot s_2^* \rangle}{\sqrt{\langle s_1 \cdot s_1^* \rangle \langle s_2 \cdot s_2^* \rangle}} \quad (2)$$

where s_1 and s_2 are complex values in image 1 and image 2, and s^* is the conjugate of s . When computing coherence of a PSC, interferograms with a baseline value greater than 1500 m are excluded for their ambiguous heights, which result from the height difference corresponding to the 2π phase change defined by Massonnet

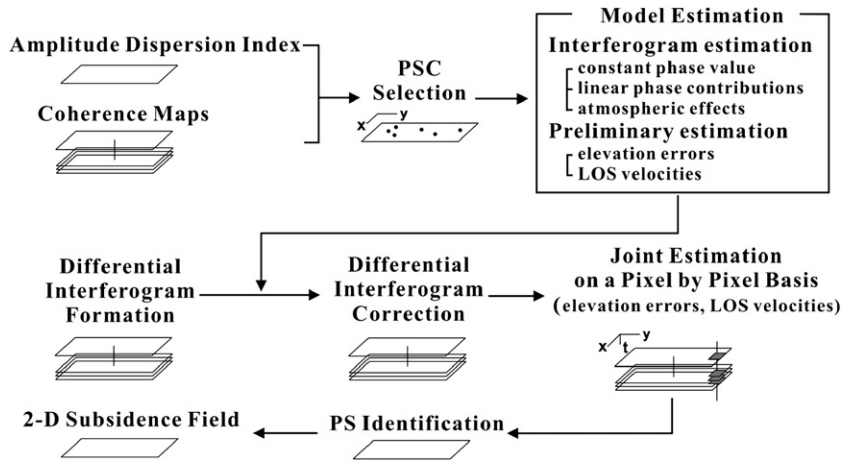


Fig. 2. Schematic diagram of the data processing procedures conducted in this study.

and Rabaute (1993), are less than 35 m. In such cases, it is difficult to preserve stable phases, even with minute errors in elevation.

PSCs were selected if ground objects satisfied both the low amplitude dispersion index and the high coherence value given by:

$$PSC_{D_A} = \{(x, y) | D_A(x, y) < 0.25\} \quad (3)$$

$$PSC_{\gamma} = \{(x, y) | \forall \gamma_i(x, y) > 0.4, b_i < 1, 500m\},$$

for $i = 1, \dots, n$ (4)

$$PSC = PSC_{D_A} \cap PSC_{\gamma}, \quad (5)$$

where (x, y) is the positional coordinate of a point target, b_i is the perpendicular baseline of the i th interferogram, and n is the total number of acquired interferograms.

3.2. Differential interferogram correction

Before conducting joint estimation of elevation errors and line-of-sight (LOS) displacements, unnecessary phase must be removed from the differential interferograms using the phase of PSCs (Ferretti et al., 2000). To correct a differential interferogram, three types of phase must be estimated and removed: Constant phase values (ϕ_{constant}), the linear phase contributions (ϕ_{slope}) of atmospheric effects and orbital fringes, and nonlinear atmospheric effects ($\phi_{\text{atmosphere}}$). The amount of phase correction was estimated from the phases of PSCs. Once constant phase values and linear phase contributions were estimated on the differential interferogram images, nonlinear atmospheric effects were then calculated by smoothing spatially the high-pass filtered phase residues. The nonlinear atmospheric effects can be interpo-

lated on the uniform image grid (Ferretti et al., 2000). Atmospheric artifacts show a strong spatial correlation within each individual SAR acquisition (Goldstein, 1995; Williams et al., 1998). This method involves an iterative and least-squares process to effectively unwrap the phase (Ferretti et al., 2001). The relationship between the original and corrected differential interferograms is defined by

$$\Delta\phi'(x, y, t_i) = \Delta\phi(x, y, t_i) - \{\phi_{\text{constant}}(t_i) + \phi_{\text{slope}}(x, y, t_i) + \phi_{\text{atmosphere}}(x, y, t_i)\}, \quad (6)$$

where $\Delta\phi$ is the original phase and $\Delta\phi'$ the phase of the corrected interferogram.

Phase correction results in the interferometric phase containing only LOS displacement, elevation error and residual noisy error. The LOS displacement rate is the line-of-sight component of the ground subsidence velocity that is of primary interest herein.

3.3. PS identification

While the persistent scatterer candidates are used for phase correction, the persistent scatterers are objects finally selected for displacement estimation (Ferretti et al., 2001). PSs are not necessarily selected from persistent scatterer candidates, but from any pixels maintaining coherent phase. The number of final PSs is usually larger than that of the PSCs. After correcting all the differential interferograms, elevation errors (∇q) and LOS velocities (v) are computed on a pixel-by-pixel basis. Phase contribution of topographic effect is proportional to the baseline (B) and the elevation error. The surface displacement projected on the radar LOS will turn into a phase curve as a function of the time interval (T) between the slave and

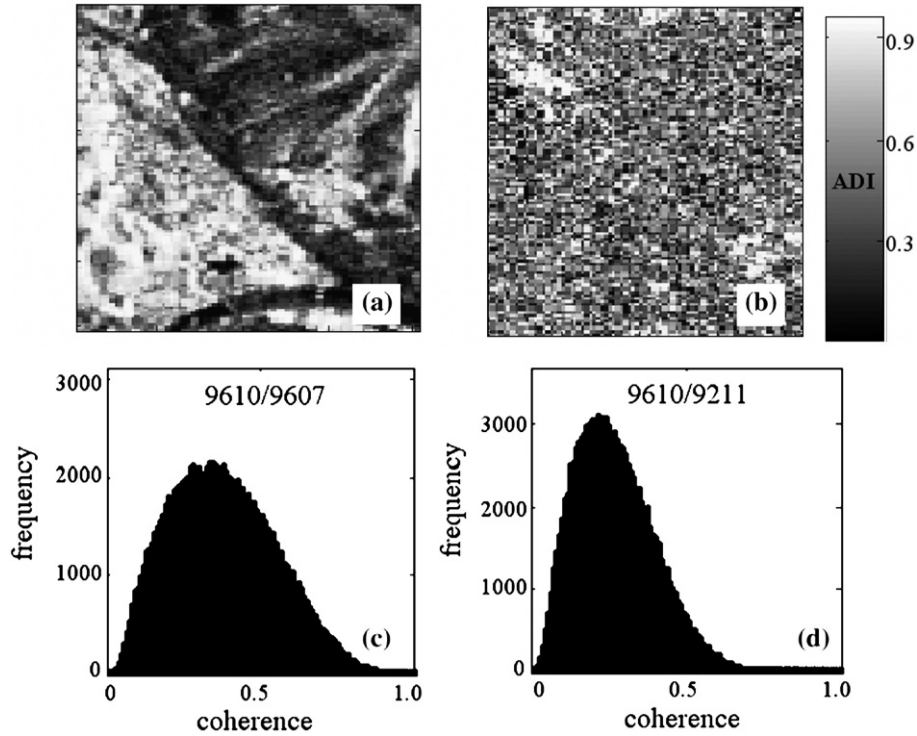


Fig. 3. Amplitude dispersion index and coherence histograms. (a) A stacked amplitude image of 26 JERS-1 SAR data and (b) amplitude dispersion index. (c) A coherence histogram of the 9610_9607 pair with a time interval of 88 days and (d) a coherence histogram of the 9610_9211 pair with a time interval of 1452 days.

master images. A constant velocity model is adopted for ground subsidence given by

$$\Delta\phi'(x, y, t_i) = T(t_i) \cdot v(x, y) + B(t_i) \cdot \nabla q(x, y) + R(x, y, t_i), \quad (7)$$

where R is the residual phase noise caused by temporal and baseline decorrelation and the effects of non-uniform pixel motion.

Provided that residual phase noise is quite small with respect to the linear model, the point can be regarded as a persistent scatterer (Ferretti et al., 2000). Phase coherence (Γ) is considered to be a reliability measure when fitting a constant velocity model and is defined by

$$\Gamma(x, y) = \left| \frac{1}{n} \sum_{i=1}^n e^{j \cdot R(x, y, t_i)} \right|. \quad (8)$$

In our implementation, a point of $\Gamma > 0.7$ is identified as PS.

3.4. Two-dimensional subsidence field

Since LOS velocity is a vector projection of ground subsidence in the line-of-sight direction, it is possible to

construct a two-dimensional subsidence field by two-dimensional interpolation of the estimated LOS velocities at the PSs. The total number of PSs identified in the study area was, however, not enough to generate a two-dimensional subsidence field. Instead of two-dimensional interpolation, we implemented a spatial smoothing of the LOS velocities using coefficients and phase coherences of a 3×3 mask. This mask template is given by

$$\text{Mask template} = \begin{array}{|c|c|c|} \hline c_1 \cdot \Gamma_1 & c_2 \cdot \Gamma_2 & c_3 \cdot \Gamma_3 \\ \hline c_4 \cdot \Gamma_4 & c_5 \cdot \Gamma_5 & c_6 \cdot \Gamma_6 \\ \hline c_7 \cdot \Gamma_7 & c_8 \cdot \Gamma_8 & c_9 \cdot \Gamma_9 \\ \hline \end{array} \quad (9)$$

We set the coefficients (c_i) to be unequally weighted, taking into account the distance to neighboring pixels: $(c_1, c_3, c_7, c_9) = 0.25$, $(c_2, c_4, c_6, c_8) = 0.5$ and $c_5 = 1.0$. The coefficients of the mask were weighted by phase coherence values (Γ_i) to emphasize high phase coherence. When a LOS velocity of the center input pixel is $v_5 = v_{x, y}$ at a given period, the convolution of the LOS velocity (v_i)

with the mask ($c_i \cdot \Gamma_i$) of Eq. (9) results in a spatial smoothing such that

$$v_{5,\text{out}} = \frac{\sum_{i=1}^9 c_i \cdot \Gamma_i \cdot v_i}{\sum_{i=1}^9 c_i \cdot \Gamma_i} \quad (10)$$

This 2-D subsidence field differs from the LOS velocity calculated directly from each PS in that the velocity in the 2-D field is spatially filtered by considering the neighboring LOS velocity. Although the resulting 2-D subsidence map is not as precise as the result directly derived from the PS phase, it aids in the review of the overall subsidence pattern in the study area.

4. Results and discussion

4.1. Measured subsidence

Twenty-five JERS-1 SAR interferometric pairs were successfully constructed. The stack of 26 JERS-1 SAR amplitude images, illustrated in Fig. 3(a), reflects physical features in the study area. In the stacked image, dark areas represent radar shadows on the rear slopes of hills or the objects of temporally random backscattering, while the bright areas represent the fore slopes of hills or the areas of consistent backscattering. A stable object produces consistent backscattering throughout the observation period and results in additive amplitude in the stacked image.

The amplitude dispersion index in Eq. (1) was calculated from the stacked image and the results are displayed in Fig. 3(b). The northwestern and southwestern parts of the image show a higher amplitude dispersion index. Fig. 3(c) and (d) present coherence histograms of the 9610_9607 pair for an 88 day time interval and that of the 9610_9211 pair for a 1452 day time interval. The mean and standard deviation of coherences for the former and latter pairs were 0.39 ± 0.17 (Fig. 3(c)) and 0.27 ± 0.12 (Fig. 3(d)), respectively. These coherence histograms show that a pair of shorter intervals produces higher coherence than that of longer intervals. It implies that coherence decreases with temporal baseline. The central part of the image is a residential area which generally produces higher coherence and a lower amplitude dispersion index, relative to the surrounding hills and mountains. Vegetation covering non-residential areas is subject to greater change during shorter time intervals than are artificial structures. A good PSC must have a small amplitude dispersion index and high coherence. Based on the amplitude dispersion index and coherence maps, twenty-two PSCs were selected in the study area.

Fig. 4 shows an example of the limitation of the amplitude dispersion index as a single criterion for PSC selection. Coherence values of three different PSCs in 15 interferograms are plotted in Fig. 4. All three scatterers had amplitude dispersion indices less than 0.25, thus satisfying the threshold value. However, the scatterer denoted by the triangle is characterized by low coherence despite its being better, in terms of its amplitude dispersion index, than the scatterer denoted by

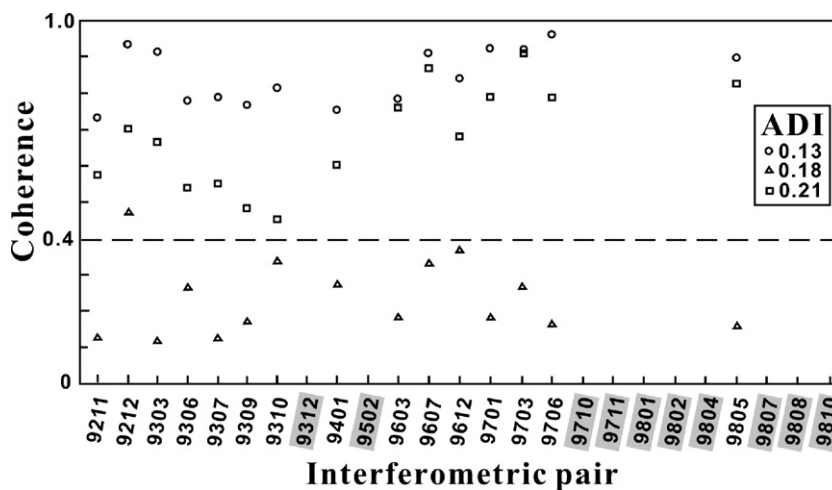


Fig. 4. An example of PSC selection with amplitude dispersion index and coherence criteria. All three scatterers satisfied the threshold of amplitude dispersion index of 0.25. Coherence of the scatterer denoted by the triangle was less than the coherence threshold of 0.4 (horizontal dashed line), so that it was removed from the PSC. Coherences were calculated by 15 interferograms whose perpendicular baselines were less than 1500 m.

square. It is necessary to determine the threshold of coherence. The standard deviation of phase σ_ϕ is defined by (Rodriguez and Martin, 1992)

$$\sigma_\phi = \frac{1}{\sqrt{2N_L}} \frac{\sqrt{1-\gamma^2}}{\gamma} \quad (11)$$

where γ is coherence in Eq. (2) and N_L is the number of looks. For this study, N_L is 27 (that is 9 azimuth looks multiplied by 3 range looks). Thus γ is 0.4 and σ_ϕ 0.31. In this study, a coherence of 0.4 is used as the coherence threshold for persistent scatterer candidates. Therefore, the scatterer with an average coherence 0.18 in Fig. 4 (triangle) was not selected as a PSC. Twenty-two of the 40 originally selected scatterers satisfied both conditions and were finalized as PSCs.

The differential interferogram was obtained by eliminating topographic effects using a published DEM. Constant phases, orbital fringes and atmospheric effects must be estimated and subtracted from the differential phases of the PSCs (see Eq. (6)). Fig. 5 shows an example of the linear and non-linear phase correction of the 9610_9703 pair. Fig. 5(a) represents the sum of the constant phase (ϕ_{constant}) and the linear phase contribution (ϕ_{slope}). The non-zero slope of the linear phase arises from imprecise orbit and atmospheric condition

data, while the constant phase is the mean of the differential interferogram, which is employed to drive the differential phase of the reference point to zero. Fig. 5(c) represents the constant and linear phase along profile AB in Fig. 5(a). The constant phase was +1.13 rad, and the linear slopes were +0.03 rad/km and +0.003 rad/km along the azimuth and slant range, respectively. Fig. 5(b) presents non-linear atmospheric effect ($\phi_{\text{atmosphere}}$). Fig. 5(d) displays a profile of non-linear atmospheric phase along A'B' in Fig. 5(b). The standard deviation of non-linear atmospheric effects was 0.09 rad.

The corrected interferogram contained a ground subsidence component, elevation error and residual errors. To obtain the subsidence rate, it is necessary to eliminate the elevation error. Joint estimation of the elevation error and subsidence rate by Eq. (7) is performed on each pixel using wrapped phases of the 25 corrected differential interferograms. LOS subsiding velocity was finally estimated for all pixels at which phase coherence was bigger than 0.7, as explained by Eq. (8). Fig. 6 shows an example of subsidence rate estimation at a persistent scatterer. Fig. 6(a) and (b) respectively display the original and corrected differential phases at a point target. The three correction terms (ϕ_{constant} , ϕ_{slope} , $\phi_{\text{atmosphere}}$) were taken from Fig. 6(a) and plugged into Eq. (6) to obtain Fig. 6(b). A regression line of differential phases

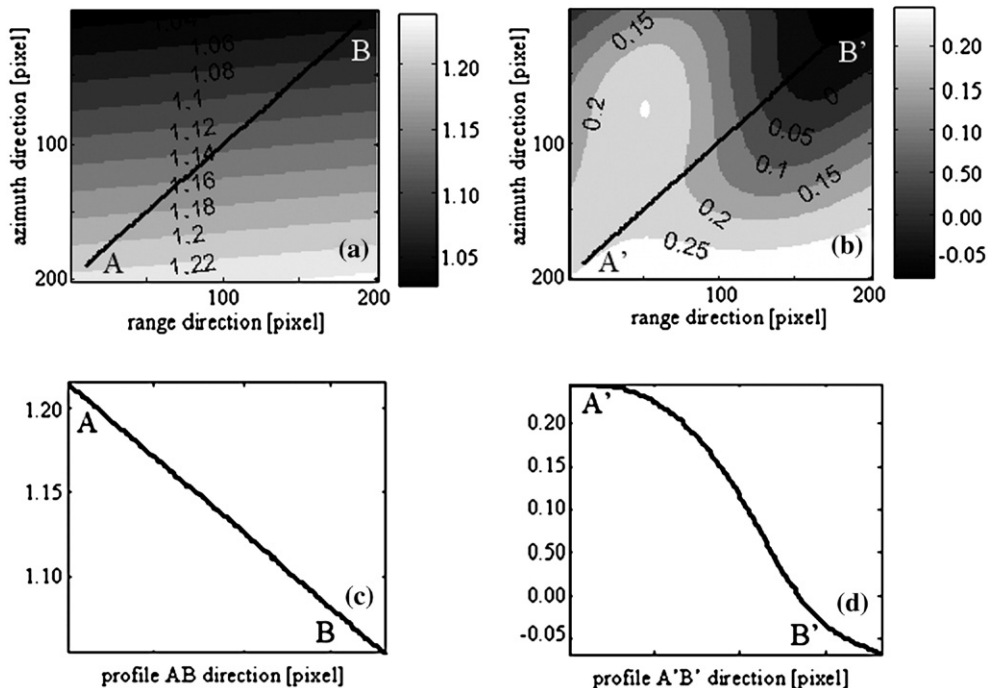


Fig. 5. An example of linear and non-linear phase correction of 9610_9703 pair. (a) Constant and linear phase contribution, and (b) non-linear atmospheric effect. (c) A profile AB of constant and linear phase, and (d) a profile A'B' of non-linear atmospheric phase.

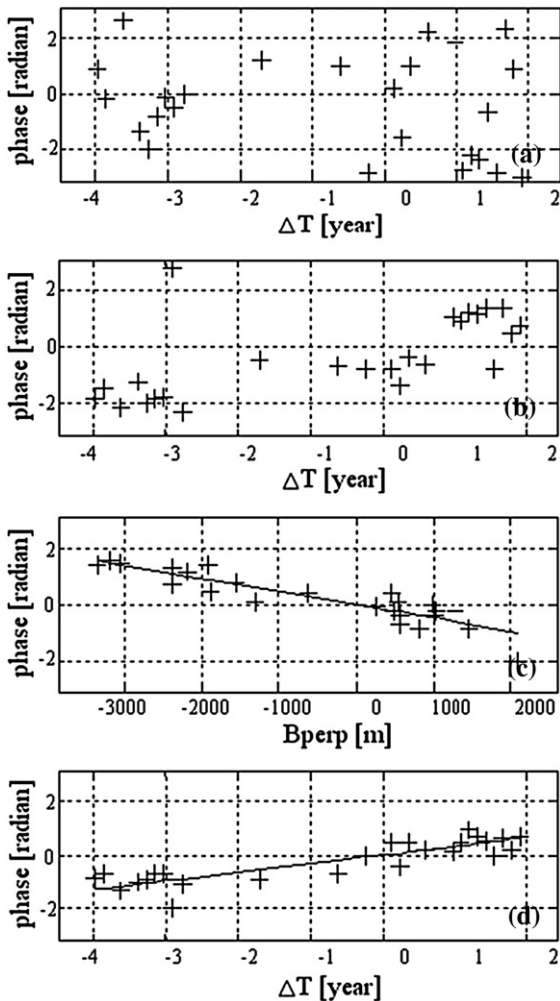


Fig. 6. An example of subsidence rate estimation at a persistent scatterer: (a) Original differential phase, (b) differential phase after linear and non-linear phase correction, (c) estimation of elevation error (4 m), and (d) final estimation of the subsidence rate (0.6 cm/yr).

with respect to the perpendicular baseline in Fig. 6(c) corresponds to the elevation error. The slope of the fitted straight line shows the elevation error to be 4 m. When the estimated elevation error is removed, the LOS subsidence rate can be obtained by a linear subsidence model, as in Fig. 6(d). The phase (φ) in radians of the y -axis in Fig. 6(d) is calculated as a distance by $dR = \lambda \cdot \varphi / 4\pi$, where λ is the wavelength of the radar signal. The wavelength of the L-band of the JERS-1 SAR is 23.53 cm. General interpretation of the result indicates that the observed ground point endured continuous subsidence at a rate of 0.6 cm/yr, for a total subsidence of 3.6 cm over 6 yr. The result shows the radar-based method to be useful for the monitoring of slow but consistent ground subsidence. However, because residual errors caused by various sources cannot be sepa-

rated, the accuracy of the estimation must depend on the residual phase noise. Still, residual errors are normally found to be very small relative to other terms.

Like the PSCs, most of the PSs were identified in residential areas; the vegetation covered hills and mountains are subject to too much temporal decorrelation, comparatively, to yield suitable PSs. Fig. 7(a) presents the location and estimated subsidence rate of each of the PSs. The number of final PSs was 135, enough to understand the ground subsidence patterns occurring across the abandoned coal mining area. Subsidence in the area was classified into five severity classes based both on the degree of crack level and the PS analysis. The color and identification number of each polygon in Fig. 7(b) and (c) are; i) G1 in red for areas classified as having a severe crack level, with cracks greater than 15 mm wide, ii) G2 in orange for areas with a moderate crack level, with cracks between 5 and 15 mm, iii) G3 in yellow for areas with a slight crack level, with cracks less than 5 mm, and iv) uncolored Gr for areas with a very slight crack level, with cracks less than 1 mm. These four groups were classified by field surveyed crack width. The polygon G4 in purple in Fig. 7(b) and (c) was originally classified as very slight crack level from the field survey in 1997. However, the current results suggested that the classification of this area be altered to be representative of a significantly subsiding area. A recent field observation confirmed that subsidence in the area is more significant than revealed by the 1997 survey. Fig. 7(c) presents the mean subsidence rate of each group and the subsidence rates of points computed by the spatial smoothing algorithm described in Section 3.4 in the two-dimensional subsidence field. The 2-D subsidence field map was useful in the review of the ground subsidence pattern in the abandoned coal mining area. In the whole study area, 7% (135 out of 1987) were identified as PSs and 36% (717 out of 1987) were shown to be meaningful points in the 2-D field map. The subsidence rate derived from the 2-D field is not always identical to that directly calculated from the PSs because of spatial filtering and smoothing. However, average subsidence rates from the two results agree with each other as summarized in Table 2. For the group G1, a mean subsidence rate of 4 PSs was 0.5 cm/yr, the same as that of 22 pixels in the 2-D field map. For groups G2 and G3, the mean subsiding rates from the PSs and 2-D fields were 0.3 and 0.2 cm/yr, respectively. A detailed comparison between the field surveyed crack level and the space-borne radar measurement will be discussed in detail in the next sub-section.

The subsidence rates measured by the PSs account for the ground subsidence at their specific positions.

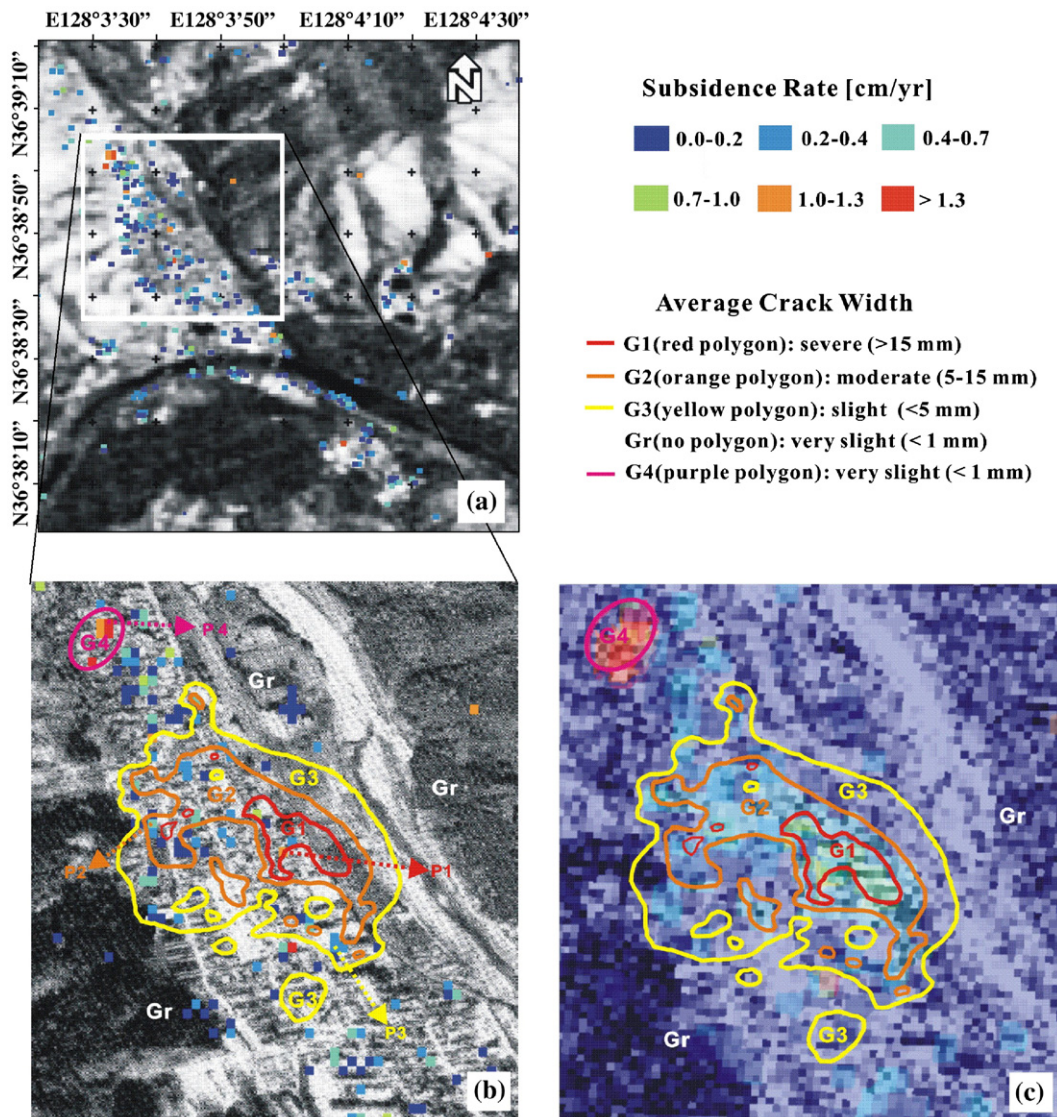


Fig. 7. Comparison between measured crack levels and estimated subsidence rate. (a) Location of the final persistent scatterers and their subsidence rates. (b) Aerial photograph overlaid with crack level and estimated subsidence rate at each persistent scatterer. (c) Two-dimensional subsidence field resulting from spatially smoothing.

Results from direct analysis of the PSs allow us to study the temporal development of ground subsidence from 1992 to 1998. Fig. 8 presents the temporal development of subsidence at the four selected PSs. The P1, P2, P3, and P4 in Fig. 7 were selected as representatives of the groups G1, G2, G3, and G4, respectively. Phase coherences of P1–P4 are relatively high at 0.74, 0.92, 0.95, and 0.83, respectively, implying that the estimation may be conducted with a high degree of confidence. In Fig. 8, the subsidence rate is a function of the gradient of the fitted line. P4 shows the highest subsidence rate among them, with an average subsidence rate of 1.9 cm/

yr and an accumulated subsidence of 11.2 cm over 6 yr. P2 and P3 produced low rates of 0.4 cm/yr and 0.2 cm/yr, respectively. The temporal development of the subsidence at P3 was the most linear of the time series. The RMS errors of the fitted line to P1–P4 were 1.38, 0.86, 0.65, and 1.14 cm, respectively.

The accuracy of the estimated subsidence rate depended on the temporal baseline distribution and the phase stability of the target given by

$$\sigma_v^2 \approx \frac{\sigma_\varphi^2}{C_v^2 \sum (T_k - \bar{T})^2} \quad (12)$$

Table 2

Summary of the radar measured subsidence rates of persistent scatterers, the 2-D subsidence field, and the field measured degree of crack level

Group (total pixels)	Persistent scatterers			2-D field		Crack level [width, mm]	Remarks
	No. of PSs	Subsidence rate [cm/yr]		No. of pixels	Subsidence rate [cm/yr]		
		Mean	Standard deviation				
G1 (44)	4	0.5	0.44	22	0.5	Severe (>15)	Areas influenced by abandoned coal mines.
G2 (176)	17	0.3	0.20	65	0.3	Moderate (5–15)	
G3 (355)	29	0.2	0.24	161	0.2	Slight (<5)	
Gr (1377)	80	0.2	0.21	444	0.2	Very slight (<1)	The rest areas of G1–G3. Gr was expected but a significant subsidence was detected by this study.
G4 (35)	5	1.7	0.55	25	1.7	?	

where σ_ϕ^2 is phase noise variance, $C_v=4\pi/\lambda$, T_k temporal baselines, and \bar{T} is the mean value of the temporal baselines (Ferretti et al., 2001). From the baselines of the pairs listed in Table 1, the estimated accuracy was 0.18 cm/yr. Consequently, subsidence in the areas of G1, G2, and G4 are confident. However, subsidence in G3 and Gr are inconclusive considering the mean subsidence rate 0.2 ± 0.24 cm/yr of G3 and 0.2 ± 0.21 cm/yr of Gr.

Although the linear PS technique model is very useful for measuring slow but continuous subsidence, the linear subsidence model could not accommodate nonlinear subsidence. Coherent scatterers undergoing a complex motion cannot be identified as PSs, or, in other cases, the non-linear term of their motion is considered as a part of the atmospheric contributions (Ferretti et al., 2000). Abrupt collapse related to calcite dissolution has been also reported in the study area, but it was not included in our analysis.

4.2. Comparison between radar measurement and degree of crack level

The estimated subsidence rates were compared with the degree of crack level obtained by a 1997 field survey. The subsidence measured by the PS technique presents an average subsidence rate over the period of image acquisition, from 1992 to 1998. Also recall that the field survey was confined to man-made structures. Table 2 summarizes the degree of crack level obtained by the field survey and the subsidence rates measured by the satellite radar system.

As shown in Table 2, the degree of crack level positively correlates with the subsidence rates calculated by both the PSs and 2-D fields. In the areas of G1, G2, and G3, which had been influenced by the abandoned mines, cracks had developed on man-made structures such as houses and buildings, roads, etc. The field

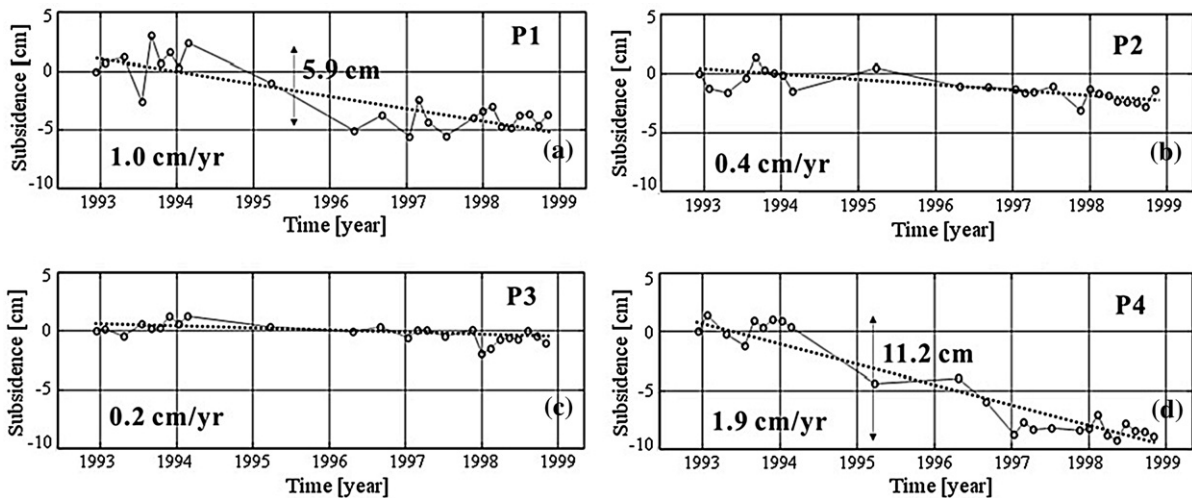


Fig. 8. These plots show the temporal development of the displacement at four selected persistent scatterers P1, P2, P3, and P4 in Fig. 7(b). (a)–(d) P1–P4 were selected as representatives of the groups G1, G2, G3, and G4, respectively. The phase coherences of P1–P4 were 0.74, 0.92, 0.95, and 0.83, respectively, and RMS errors of the fitted line to P1–P4 were 1.38, 0.86, 0.65, and 1.14 cm, respectively.

surveyed crack widths were over 15 mm in the area of G1, 5 to 15 mm in G2, and less than 5 mm in G3. As confirmed by Table 2 and Fig. 7(b) and (c), field measurements in the areas of G1, G2 and G3 well agreed with radar measurements. The area classified as Gr by field survey is representative of very slightly damaged or intact areas near underground coal mines. The crack widths in the Gr area were less than 1 mm in field observation. However, as a result of this study, and as shown in Fig. 7(b) and (c), an area categorized as Gr during the 1997 field survey was shown to have actually endured significant subsidence during the period of radar measurement. Subsidence in the G4 area was limited to a small area without man-made structures. The field survey in 1997 was focused only on man-made structures, so ground subsidence in the foothills was not taken into account.

Building damage due to excavation-induced ground movement has been investigated using a damage criterion based on the average state of strain in the distorting portion of the structure (Son and Cording, 2005). Building damage in terms of cumulative crack width determined from strains was evaluated by Boone et al. (1998). It is usually the portion of the building closest to the excavation and subject to the largest distortions. The strain in the plane of a building wall is determined by measuring the vertical and lateral displacements at the four corners of a section of the wall. The displacements in the study were calculated by PS technique and building damage was evaluated by the degree of crack level measured in situ. Fig. 9 shows a relationship between the subsidence rate of PSs and crack level of each group. The mean PS-derived subsidence rates with standard deviation bars were plotted with respect to groups classified by the degree of crack width. The obtained subsidence rate was shown to be well correlated with the crack width, save for group Gr. The discrepancy at Gr can be explained by the sub-

sidence that went unrecorded during the 1997 field survey due to man-made structures being scattered or absent. Fig. 9 shows that crack level in the study area could be a good indicator of ground subsidence.

The subsidence rates measured by PS technique has been shown to agree well with the crack level data, and thus be useful for continued monitoring of the abandoned coal mining area. Since the population in the area is relatively low, and because damage induced by ground subsidence has been limited, building damage may be adequately assessed by field survey. However, should it become necessary to review the entire region in preparation for the construction of a new highway or railroad, the proposed radar method may prove more thorough and useful. Although we were not able to directly compare the total amount of subsidence measured by space-borne SAR with the ground measured data, results demonstrate that the PS technique is an effective tool for monitoring ground subsidence triggered by underground mines in mountainous regions.

5. Conclusions

Persistent scatterer SAR interferometry was applied to measure subsidence in an abandoned coal mining area from November 1992 to October 1998. A maximum of 11.2 cm of ground subsidence occurred over 6 yr in the study area. The SAR measurements were compared with crack levels collected during a 1997 field survey. The field observation divided building damages into four groups according to the average crack width; G1 (>15 mm), G2 (5–15 mm), G3 (<5 mm), and Gr (<1 mm). While the field survey was confined to the observation of man-made structures, the space-borne SAR measurements were obtained from natural ground and artificial structures. Consequently, the two results do not always match. Nevertheless, the radar measured subsidence showed good agreement with the order of crack level. The average subsidence rates in the G1–G3 classes were of 0.5 cm/yr, 0.3 cm/yr and 0.2 cm/yr, respectively. From the SAR measurements, one group determined by field survey to have endured minimal subsidence, G4, was added as an area of significant subsidence (1.7 cm/yr). The crack width obtained by field survey was well correlated with the radar measurement, validating that the PS technique is an effective tool for monitoring abandoned coal mining areas, even in mountainous regions. Despite the low density of persistent scatterers, it was possible to construct a two-dimensional subsidence map. The 2-D subsidence map is aids in our understanding of the regional pattern of subsidence in the study area.

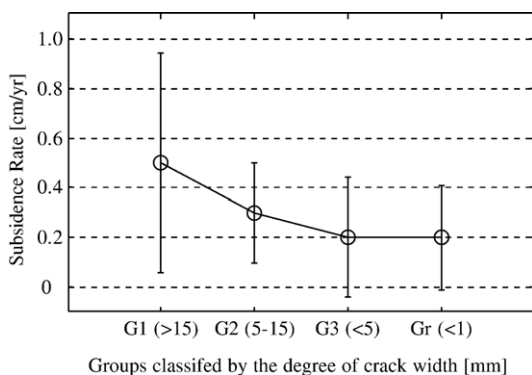


Fig. 9. Comparison of obtained subsidence rates and crack levels.

Results demonstrate the potential of L-band PS technique for measurement of ground subsidence in mountainous areas. Compared with the C- or X-bands, the L-band is able to account for rapid subsidence due to its longer wavelength. As such, L-band PS technique could be useful in the observation of landslides as well as ground subsidence. Although the adopted method effectively detected and measured ground subsidence, it is limited to the observation of continuous and temporally linear subsidence. To precisely measure non-linear subsidence, it is necessary to develop a more sophisticated non-linear subsidence retrieval model suitable to the subsiding nature of abandoned coal mines.

Acknowledgment

JERS-1 SAR datasets were provided in part by JAXA under ALOS Program (PI No. 120). We thank the Korean Mine Reclamation Co. for supplying the field survey data and Dr. Bok Chul Kim (Korea Institute of Geoscience and Mineral Resources) for invaluable comments on geology. We also thank the POLIMI SAR group for their works. Finally, we thank two anonymous reviewers for their helpful comments.

References

- Alsdorf, D.E., Melack, J.M., Dunne, T., Mertes, L.A.K., Hess, L.L., Smith, L.C., 2000. Interferometric radar measurements of water level changes on the Amazon flood plain. *Nature* 404, 174–177.
- Berardino, P., Fornaro, G., Lanari, R., Sansosti, E., 2002. A new algorithm for surface deformation monitoring based on small baseline differential SAR interferograms. *IEEE Transactions on Geoscience and Remote Sensing* 40, 2375–2383.
- Berardino, P., Costantini, M., Franceschetti, G., Idoice, A., L.Pietranera, V., 2003. Use of differential SAR interferometry in monitoring and modeling large slope instability at Maratea (Basilicata, Italy). *Engineering Geology* 68, 31–51.
- Boone, S.J., Westland, J., Nusink, R., 1998. Comparative evaluation of building response to an adjacent braced excavation. *Canadian Geotechnical Journal* 36, 210–223.
- Bruhn, W.R., Speck, R.C., Thill, R.E., 1983. The Appalachian field: damage to structures above active underground mines. *Surface Mining Environmental Monitoring and Reclamation Handbook*. Elsevier, New York, pp. 656–669.
- Carnec, C., Delacourt, C., 2000. Three years of mining subsidence monitored by SAR interferometry, near Gardanne, France. *Journal of Applied Geophysics* 43, 43–54.
- Coal Industry Promotion Board, 1997. Geological and principal research for the ground stability assessment on the mined-out area in Munkyeong Region.
- Colesanti, C., Ferretti, A., Prati, C., Rocca, F., 2001. Comparing GPS, optical leveling and persistent scatterers. *Proceedings of IGARSS 2622–2624*.
- Colesanti, C., Ferretti, A., Ferrucci, F., Prati, C., Rocca, F., 2003. Monitoring landslides and tectonic motions with the persistent scatterers technique. *Engineering Geology* 68, 3–14.
- Demoulin, A., Campbell, J., Wulf, A., Muls, A., Arnould, R., Gorres, B., Fischer, D., Kotter, T., Brondeel, M., Damme, D., Jacqmotte, J., 2005. GPS monitoring of vertical ground motion in northern Ardenne–Eifel: five campaigns (1999–2003) of the HARD project. *Journal of Earth Sciences* 94, 515–524.
- Ferretti, A., Prati, C., Rocca, F., 2000. Nonlinear subsidence rate estimation using permanent scatterers in differential SAR interferometry. *IEEE Transactions on Geoscience and Remote Sensing* 38 (5), 2202–2211.
- Ferretti, A., Prati, C., Rocca, F., 2001. Permanent scatterers in SAR interferometry. *IEEE Transactions on Geoscience and Remote Sensing* 39 (1), 8–20.
- Goldstein, R.M., 1995. Atmospheric limitations to repeat-track radar interferometry. *Geophysical Research Letters* 22 (18), 2517–2520.
- Jonsson, S., Zebker, H.A., Cervelli, P., Segall, P., Carbeil, H., Mouginis-Mark, P., Rowland, S., 1999. A shallow-dipping dike fed the 1995 flank eruption at Fernandina Volcano, Galapagos: observed by satellite radar interferometry. *Geophysical Research Letters* 26 (8), 1077–1080.
- Kim, S.W., Measurement of Surface Displacement of Mt. Baekdu and Busan Area Using L-band SAR Interferometry, Ph.D. dissertation of Yonsei University, 2004.
- Kim, S.W., Lee, C.W., Song, K.Y., Min, K.D., Won, J.S., 2005. Application of L-band differential SAR interferometry to subsidence rate estimation in reclaimed coastal land. *International Journal of Remote Sensing* 26 (7), 1363–1381.
- Massonnet, D., Rabaute, T., 1993. Radar interferometry — limits and potential. *IEEE Transactions on Geoscience and Remote Sensing* 31, 455–464.
- Massonnet, D., Rossi, M., Carmona, C., Adragna, F., Peltzer, G., Fiegl, K., Rabaute, T., 1993. The displacement field of the Landers earthquake mapped by radar interferometry. *Nature* 364, 138–142.
- National Coal Board (NCB), 1975. Mining Department, Subsidence Engineers Handbook.
- Rodriguez, E., Martin, J.M., 1992. Theory and design of interferometric synthetic aperture radars. *IEEE Proceedings—F Radar and Signal Processing* 139, 147–159.
- Sneed, M., Ikehara, M., Balloway, D., Amelung, F., 2001. Detection and measurement of land subsidence using global positioning system and interferometric synthetic aperture radar, Coachella Valley, California, 1996–1998. *Water-Resources Investigations Report 01-4193*, US Geological Survey, USA.
- Son, Moorak, Cording, E.J., 2005. Estimation of building damage due to excavation-induced ground movements. *Journal of Geotechnical and Geoenvironmental Engineering* 131, 162–177.
- Steve, B., Kuipers, J., 2002. Technical report on underground hard-rock mining: subsidence and hydrologic environmental impacts. *The center for Science in Public Participation*, pp. 2–41.
- Suzanne, L., Sandwell, D., 2003. Fault creep along the southern San Andreas from InSAR, permanent scatterers, and stacking. *Journal of Geophysical Research* 108 (B1), 2047. doi:10.1029/2002JB001831.
- Usai, S., 2003. A least squares database approach for SAR interferometric data. *IEEE Transactions on Geoscience and Remote Sensing* 41 (4), 753–760.
- Williams, S., Bock, Y., Fang, P., 1998. Integrated satellite interferometry: tropospheric noise, GPS estimates and implications for interferometric synthetic aperture radar products. *Journal of Geophysical Research* 103 (B11), 27051–27068.
- Wright, P., Stow, R., 1999. Detecting mining subsidence from space. *International Journal of Remote Sensing* 20 (6), 1183–1188.
- Zebker, H., Villasenor, J., 1992. Decorrelation in interferometric radar echoes. *IEEE Transactions on Geoscience and Remote Sensing* 30, 950–959.